Impact of H_2 in biogas flame-wall interaction for thermoelectric power generation

Miguel D. Santos
miguel.d.d.santos@tecnico.ulisboa.pt

Instituto Superior Técnico, Universidade de Lisboa, Portugal
November 2020

ARTICLE INFO

Keywords:
Thermoelectric generator
Flame-wall interaction
Particle image velocimetry
Chemiluminescence
Quenching distance

ABSTRACT

In this work, the viability of using premixed biogas+H_2 flames together with a thermoelectric generator (TEG), for direct heat-to-electricity conversion, was studied. We aimed to understand the influence from different fuel blends and flame conditions in TEG working temperatures and operating point. In the setup used, a TEG module contacts a wall of a combustion chamber, where a flame stabilizes in side wall quenching. The major challenges for power and efficiency optimization were found to be related with the heat transfer from flame and burnt gases to the wall and TEG. Gases velocity field, flame quenching and heat release rate (HRR) were hence studied via PIV and the chemiluminescence of excited OH* and CH* radicals. A mathematical model was developed to predict TEG operation for the different fuel and flame conditions, resorting to the finite volume method and a neural network. Its results correlated well with experimental ones ($R^2 > 0.97$), with a small over-prediction.

Even in small amounts (up to 20% in volume), we found that H_2 addition to biogas (BG) improved both TEG operation (power yielded increased by 10%) and flame stabilization (quenching distance d_q was reduced by 18%, to levels typical of methane). The impact of H_2 was more significant for the lower BG grades, which emphasized its importance for BG use in smaller, portable applications, with downsized combustion chambers (where the importance of flame-wall interaction is bigger). Correlations between chemiluminescence, HRR and d_q were deduced: it was found OH* chemiluminescence to be strongly related with d_q and convection to contribute in the same order of magnitude as conduction for heat transfer in the quenching region.

1. Introduction

The technological development has led to an increasing demand for energy worldwide. In 2019, only *ca.* 50% of the total energy produced was consumed and only *ca.* 40% of the energy designated to power plants was converted into electricity [1], which reinforces the importance of studying energy management and conversion processes. Fuels remain important energy sources, valued for their high energy density. However, with the awareness of global warming and need for decarbonizing energy systems, renewable fuels have drawn attention recently. Biomass anaerobic digestion is a powerful waste management tool: it avoids soil and water contamination, at the same time that, by capturing gas (called biogas or BG) from decomposing biomass, avoids air pollution. BG is mainly composed of CH_4 and CO_2. Carbon dioxide is responsible for biogas poor combustion properties and hence is often removed in industrial processes [2]. Since that is not always possible, the addition of small quantities of H_2 (another renewable fuel) has been a focus of study in recent years, to permit the direct use of raw biogas.

Electricity is an important form of energy that is still of difficult access in rural areas (not connected to the grid) and in activities isolated from communities (expeditions, hiking, camping). Thermoelectric generators (TEGs) are devices capable of direct heat-to-electricity conversion. The constant technological advances made them more competitive and suitable to integrate new energy management and conversion processes [3]. We believe they have a say in integrating portable and compact solutions for the decentralization of power generation, using a small flame as heat source.

The use of BG flames in smaller combustion chambers (that portable devices entail) encompasses challenges regarding flame-wall interaction (FWI). Quenching is a FWI phenomena that refers to flame extinction near the combustion chamber walls, due to heat losses and/or radical recombination reactions. FWI is important across several combustion applications, for influencing flame stabilization, acoustics, combustion chamber lifetime or even pollutants formation. For the application here studied, it will largely influence the amount of heat transfer from flame to the thermoelectric (ultimately affecting power and efficiency yielded).

Due to (i) small time and length scales, (ii) strong temperature and species concentration gradients and (iii) ambiguity in defining flame front boundaries, there is a consensus in scientific community to consider FWI a complex process, difficult to model and study experimentally.

In this paper, FWI of premixed laminar BG+H_2 flames will be studied, with the particular application to thermoelectric power generation. Methods to monitor TEG performance will be described. Particle Image Velocimetry (PIV) and chemiluminescence (of CH* and OH* excited radicals) will be used to extract information about flow-field, quenching distances and heat release in the flame near the quenching zone. The last two proved to be dependent and important correlations were obtained from those. As an important step in any type of engineering work, some remarks regarding results uncertainties are also presented.

2. Burner and TEG setup

Different experimental setups were used for diagnosing thermoelectric generator (TEG) performance and flame wall interaction; three can be distinguished: (i) power and tem-

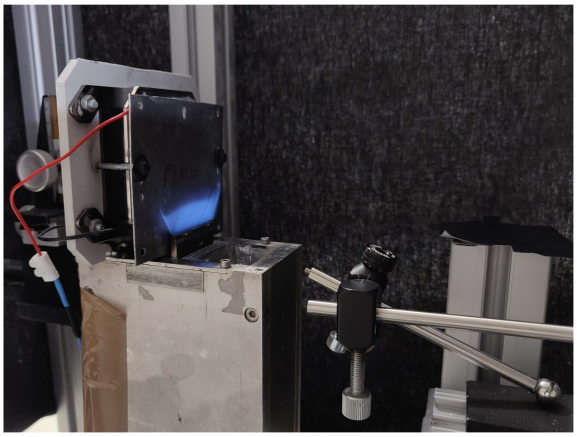

Figure 1: Experimental setup.

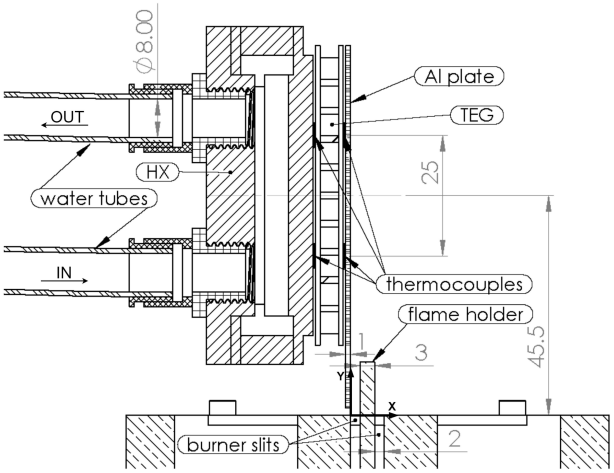

Figure 2: Details and dimensions of burner, TEG and Al plate (units in mm); XYZ cartesian coordinate system considered for experimental results.

Table 1
GM200-49-45-30 thermoelectric general characteristics.

Dimensions (mm)	$62 \times 62 \times 5.8$	
Maximum temperature:	$T_{H,max} = 200\,°C$	$T_{C,max} = 175\,°C$
Performance for:	$T_H = 200\,°C$,	$T_C = 30\,°C$
Rated output power	7.5 W	
Matched load resistance	$0.28\,\Omega \pm 15\%$	
Open circuit voltage	2.8 V	
Heat flow in TEG	~ 149 W	

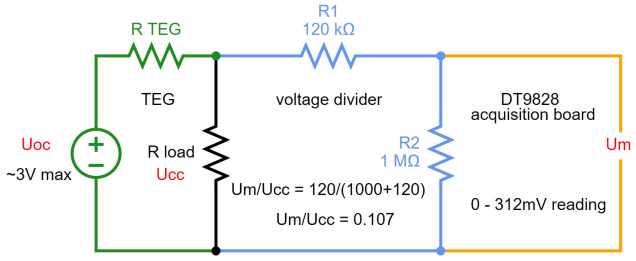

Figure 3: Electric circuit; from left to right: TEG electrical equivalent, voltage divider circuit, DT9828 acquisition board.

perature acquisitions, (ii) particle image velocimetry (PIV) for perceiving flow velocity field, and (iii) chemiluminescence setup for analyzing flame structure, quenching distances and heat release rate (HRR).

The laminar flame stabilizes on a lamella burner with two slits (40×2mm - $l \times w$) and a stainless steel flame holder (Figure 1), acquiring a 2D V-shape. Side Wall Quenching (SWQ) occurs as one of the flame branches approaches the surface of an Aluminium (Al) plate ($90 \times 75 \times 1$mm), positioned 2 mm apart from the flame holder (Figure 2) and henceforth designated by wall.

The TEG is placed between the wall and a CPU-adapted heat exchanger (HX) (Phanteks Glacier C350i), which serves as the system heat sink. Table 1 contains information about the GM200-49-45-30 (European Thermodynamics) TEG. It is positioned above the flame holder height, to be in contact with the hottest region of the wall. To diminish the thermal contact resistances between wall, TEG and HX, a thermal paste (AG Termopasty HPX) with a thermal conductivity of 2.8 W m^{-1} K was used; its dielectric constant of 5.1 ensures it does not affect the thermocouples readings. The mentioned components are fixed with bolts to a 3D printed piece (Figure 2), facilitating its change between different analysis.

Tap water is supplied through a tube connected to the bottom of the heat exchanger. The water exits in the same manner, from the top of the HX, after passing through a series of fins. For a water flow of 1.619 LPM, it has an estimate head loss of 0.945 m of water based on experimental tests.

Six OMEGA *K-type* thermocouples and a DataTranslation DT9828 acquisition board were used to monitor system temperatures: four of the thermocouples are placed in the hot and cold sides of the TEG (two on each side), 25 mm apart in the y direction (Figure 2) and at $z = 0$ plane. The other two thermocouples are placed right before (after) the inlet (outlet) of the HX. The acquisition board is connected to a computer, where data is visualized and exported using QuickDAQ software.

The TEG terminals are connected to an electric load, composed of ceramic resistances, which help improve the closed circuit voltage (U_{cc}) stability in steady state operation. Based in TEG datasheet information, the electric load was dimensioned to have a resistance always above TEG's matched one, *i.e.* $R_{e,load} > R_{e,TEG}$. This ensures that we are working always beyond the maximum power point and, consequently, that the variation of power with the heat across the TEG is monotonic. It diminishes the complexity of variables, avoiding erroneous reasoning and inferences from obtained measurements. The final measured resistance value was $R_{e,load} = 0.281\,\Omega$.

The closed circuit voltage U_{cc} was also monitored, using the same acquisition board and software described for the thermocouples. A voltage divider circuit was connected in parallel with TEG's terminals, since the acquisition board analog inputs can only handle voltages up to 312 mV. Figure

Table 2
Overview of fuels and operating conditions tested.

Reynolds number, Re	100, 150, ..., 300, 350
Equivalence ratio, ϕ	0.7, 0.8, 0.9, 1.0
Base fuels H_2 dope	BG100, BG80, BG60 0%, 10%, 20%
Min flame power, $P_{flm,min}$ Max flame power, $P_{flm,max}$	~ 263 W ~ 1387 W
Water flow rate in the HX, $\dot{V}_{H_2O}$	1.25 LPM

3 contains a scheme of the electrical circuit used. The measured voltage in the acquisition board, denoted U_m, is nearly 10 times smaller than U_{cc}.

The different flame conditions are obtained using four Alicat Scientific M-series gas flow meters, one for each gas. After being dried and filtered, air passes through a flow meter with a capacity of 50 SLPM. CH_4 and H_2 are drawn from gas bottles (Air Liquid Alphagaz 99.95%). Their flow meters have a maximum capacity of 5 SLPM and 1 SLPM respectively. Finally, CO_2, also drawn from a gas bottle (Air Liquid 99.95%), can have a maximum flow rate of 5 SLPM. The mixture is blended in a small chamber, which then connects to the burner using a single tube. The water flow rate in the HX is controlled using an Alicat Scientific LCR flow meter with 2 LPM capacity.

The flow meters set points were defined through a in-house designed LabView software, that allowed to compute each gas flow rate directly from type of fuel, Reynolds number (Re) and mixture equivalence ratio (ϕ) conditions.

For the experiments, several fuels, flame conditions and hydrogen concentrations were used (Table 2). Biogas mixtures were simulated with a blend of $CH_4 + CO_2$, since these gases account for more than 95% of the composition of BG produced by anaerobic digestion [2]. Pure methane (BG100) and two types of biogas fuels were used. For a mixture termed BG**X** **Y**%H_2, the molar fraction χ of each specie can be calculated through:

$$\chi_{H_2} = \mathbf{Y}/100 \tag{1}$$

$$\chi_{CH_4} = \mathbf{X}\,(1 - \chi_{H_2}) \tag{2}$$

$$\chi_{CO_2} = 1 - \chi_{H_2} - \chi_{CH_4} \tag{3}$$

The Reynolds numbers tested range from 100 to 350. In the lower limit the flame is small and close to flashback. In the upper limit the flame tips are close to resonate. Three lean and a stoichiometric equivalence ratios were chosen. For not affecting TEG performance significantly, water flow rate in the HX was fixed in $\dot{V}_{H_2O} = 1.25$ LPM. This simplified the analysis by reducing the number of variables.

The burner Reynolds number is defined with a characteristic length equal to the burner slit width $w = 2$ mm, and described by the equation:

$$Re = \frac{V \times w}{\nu_u} = \frac{[\dot{V}_u/(w \times l)] \times w}{\nu_u} = \frac{\dot{V}_u}{l \times \nu_u} \tag{4}$$

where $\dot{V}_u$ is the unburnt mixture volumetric flow rate, ν_u represents the mixture kinematic viscosity and $l = 40$ mm is the burner slit length. V is the mean velocity of the gases at the slit exit.

The unburnt gases exiting the burner were assumed to be at room temperature $T_u = 298.15$ K and at atmospheric pressure. To calculate the volumetric flow rate at STP conditions (used in flow meters) the ideal gas law $p = \rho_u RT$ was employed. The flame power P_{flm} was calculated from the mixture low heating value (LHV) and unburnt mixture density (ρ_u):

$$P_{flm} = LHV \times \rho_u \times \dot{V}_u \tag{5}$$

The Cantera [4] Python module was used to calculate different mixture properties. Whenever calculating dynamic viscosity, thermal conductivity or other transport quantity, the GRI-Mech3.0 [5] mechanism was used, taking into consideration the transport properties of each species individually.

3. TEG performance measurement

The direct measurement of electrical current I_e through the electrical load To calculate power yielded P_{TEG} is impractical since $R_{e,load}$ value is small. For that reason, the precise determination of $R_{e,load}$ and measurement of closed circuit voltage U_{cc} was used instead. The load resistance terminals were connected to a current generator to ensure that the load would maintain a stable and constant resistance over time, for different currents. This allowed at the same time the precise measurement of $R_{e,load}$. P_{TEG} can be estimated using the formula:

$$P_{TEG} = U_{cc} \times I_e = U_{cc} \times \frac{U_{cc}}{R_{e,load}} = \frac{U_{cc}^2}{R_{e,load}} \tag{6}$$

This same method is used by other authors to evaluate the electric output of the TEG [6].

In the computer, the analog input channels of the acquisition board were configured for the *K-type* thermocouples and for the characteristics of the voltage divider circuit, enabling the direct and continuous monitoring of power and temperature. The acquisitions lasted 3 min each, with a 5 min interval between them to ensure steady state condition was attained.

The heat rejected in the TEG in the cold side (q_C) was assumed to be absorbed by the water in the HX, increasing its temperature from $T_{H_2O,in}$ to $T_{H_2O,out}$:

$$q_C \approx \dot{m}_{H_2O}\, c_{H_2O}\, (T_{H_2O,out} - T_{H_2O,in}) \tag{7}$$

where $\dot{m}_{H_2O}\,[\mathrm{kg\,s^{-1}}] = \dot{V}_{H_2O}\,[\mathrm{LPM}] \times \rho_{H_2O}/(1000 \times 60)$ denotes the water mass flow rate and c_{H_2O} the water specific heat ($4180\,\mathrm{J\,kg^{-1}\,K^{-1}}$).

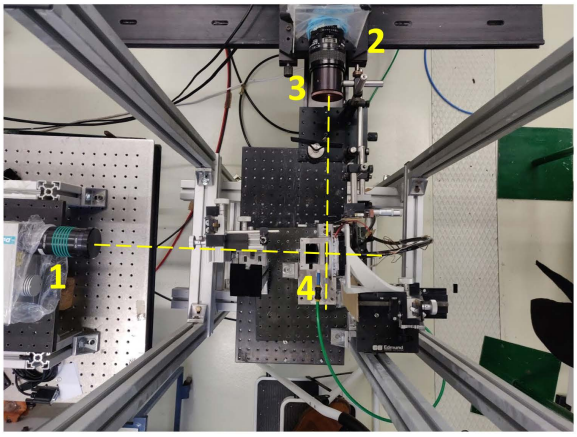

Figure 4: Top view of PIV experimental setup, showing (1) laser, (2) camera and lens, (3) 532 nm optical filter, and (4) main setup shown in Figure 1.

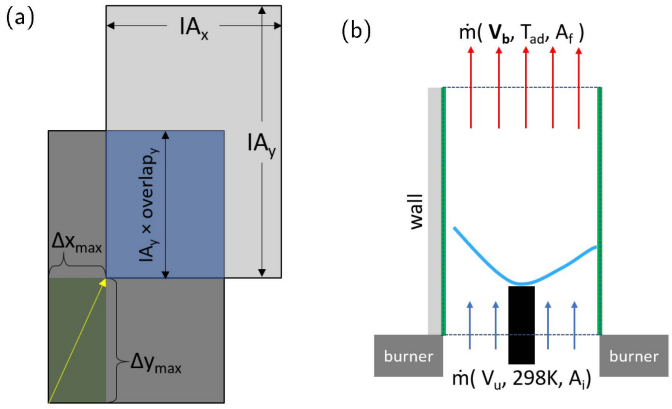

Figure 5: PIV methodologies to estimate the required time interval between frames Δt; (a) particle displacements smaller than the region defined by $\Delta x_{max} \times \Delta y_{max}$ in the IA ensure particles are detected between frames; (b) to predict $V_{y,max}$, burnt gases are assumed to reach T_{ad} in a confined control volume.

4. Flow velocity field

Aluminium oxide (Al_2O_3) particles were used as tracers for their inertness and high melting point, needed when studying combustion reactive flows. Their diameter of 1 µm and density of 3950 kg/m^3 led to an estimate Stokes number in the order of 10^{-4}, which is below the maximum advised value of 0.1 [7] hence having a sufficient response time for the flow characteristics.

An ANDOR Zyla 5.5 sCMOS camera, combined with a Nikon AF Nikor 60mm f/2.8D lenses, was used to capture particle images (Figure 4). The camera, with 5.5MP, is capable of double-frame acquisitions at 15 Hz.

The Dantec DualPower 65-15 Nd:YAG laser was used to illuminate the Al_2O_3 particles with a 532 nm laser beam. The laser sheet intensity profile is Gaussian distributed to avoid complete black-out of particles with velocity component perpendicular to plane. Whenever acquisitions with a flame were performed, a 532 nm CVI Melles Griot light filter (3 nm bandwidth) was used (transparent only to the scattered light from illuminated particles).

Finally, the laser and camera were connected to a synchronizer (BNC Model 575). The camera acquisitions were processed in a computer with the Dantec DynamicStudio v5.1 [8] software.

The camera lens was used with the aperture set to its maximum ($f/2.8$) to capture sufficient light from particles, have a shallow depth of field and use small exposure times (avoiding the blur of particles). The focus plane was set away from the minimal focal length, to diminish the optical aberrations. It was found that the resolution of 33.2 pix/mm ($res = 30.12$ µm/pix), with a magnification factor of $M = 4.607$, was adequate to capture the flow in detail and avoid pixel locking (particle Airy disk diameter D_{Airy} smaller than a single pixel), which introduces large uncertainties. The region of study took an approximate area of 25 mm × 50 mm. This led to a small characteristic time scale: for some flame conditions, it would take 1/60s for a particle to travel across the mentioned region of interest. Therefore, the temporal resolution was set to be the smallest possible (15 Hz).

Since the flow is studied in an Eulerian description, it is fundamental to define interrogation areas. Their pixel size $[\mathrm{IA}_x, \mathrm{IA}_y]$, velocity vector $\vec{V}$, image resolution (res) and overlap percentage between interrogation areas $[o_{\mathrm{IA},x}, o_{\mathrm{IA},y}]$ dictate the required time interval between frames Δt

$$\Delta t < \min\left(\frac{[\mathrm{IA}_x, \mathrm{IA}_y] \times \left(1 - [o_{\mathrm{IA},x}, o_{\mathrm{IA},y}]\right)}{[V_x, V_y] \times res}\right) \quad (8)$$

for the particles movement not to be lost between frames. Δt should then be the minimum of the two possible values that result from the piece-wise multiplication and division of the vectors presented. As Figure 5a illustrates, when particle displacements are smaller than a bounding region (constrained by Equation 8) inside the IA, it is guaranteed their movement is not lost between frames.

A IA size was firstly defined in $[\mathrm{IA}_x, \mathrm{IA}_y] = [16, 32]$ since it was expected $V_y > V_x$. A maximum value for V_y was predicted considering a mass balance in a control volume, in which burnt gases were not allowed to expand in x direction and would reach the adiabatic flame temperature (Figure 5b). The burnt gases velocity is given by:

$$V_b = V_u \times \frac{\rho_u}{\rho_b} \times \frac{A_i}{A_f} \quad (9)$$

The interrogation areas overlap was set to $o_{IA} = 50\%$ both in x and y directions.

Since the IA size and IA overlap were fixed in Equation 8, different values of V_b translated into different Δt. The time between frames was chosen to be 50 µs, 75 µs or 100 µs, whichever was closer to the value of Δt calculated for each condition.

A pre-processing of images (Figure 6), prior to the cross-correlation between frames, allowed to obtain more particle contrast and hence more and better correlations. Since the

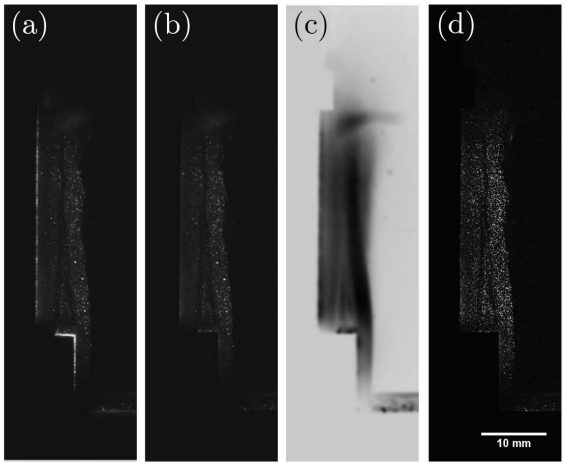

Figure 6: PIV pre-processing of (a) raw image involved: (b) the black-out of regions not to analyze, (c) filter applied to minimize unbalanced brightness and correct light sheet non-uniformity, and (d) top-hat Gaussian filter to enhance and homogenize particles contrast.

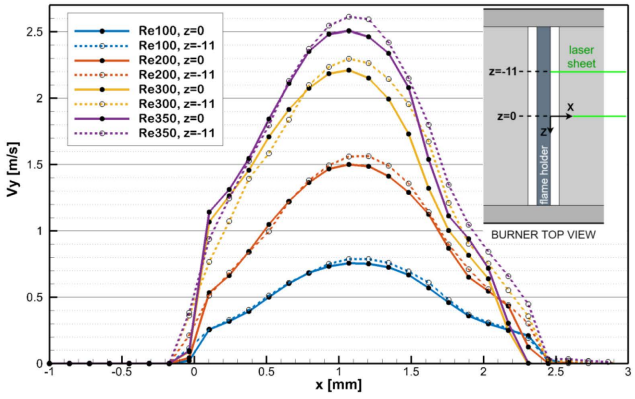

Figure 7: PIV isothermal tests; vertical velocity (V_y) profiles measured at $y = 2$ mm for two different z planes, without the wall; burner top view (inset).

flow is statistically steady, average correlation was employed to analyze the 200 pairs of frames acquired. This process automatically despises weak correlations (that may arise from insufficient particle density in some frames) and sporadic erroneous correlations (that are not consistent throughout the frame pairs).

Preliminary tests were conducted in isothermal conditions, both with and without the wall, in two different z coordinates. Those intended to evaluate if the flow could be, in fact, be described as two dimensional. The obtained results validated the methodology described so far and, as can be observed on Figure 7, verified that the velocity profiles do not change considerably along z coordinate. Taking these into account it is possible to assume that, in the plane of study:

$$\left.\frac{\partial \vec{V}}{\partial z}\right|_{z=0} \approx 0 \tag{10}$$

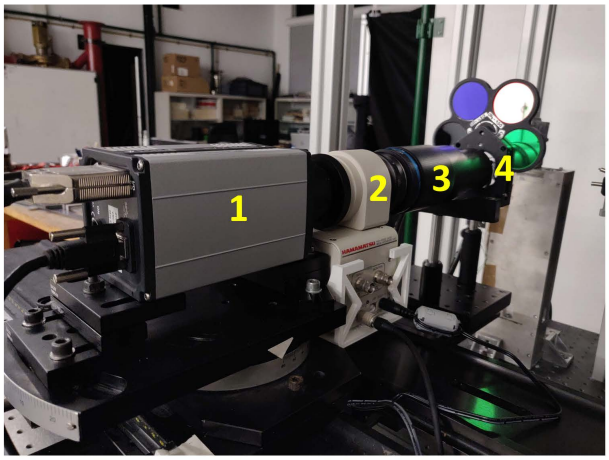

Figure 8: Chemiluminescence experimental setup with (1) camera, (2) image intensifier, (3) camera lens, and (4) optical filters.

$$\left.\vec{V}\right|_{z=0} \approx [V_x, V_y, 0] \tag{11}$$

5. Quenching Distances and Flame Structure

In this setup, the same camera, synchronizer and software described for the PIV were used. To capture the radicals chemiluminescence, a Coastal Optics 105mm f/4.5 UV-Micro-APO camera lens, which is permeable to the UV light, was used (Figure 8). An image intensifier (Hamamatsu C9547-03L3) was placed between lens and camera. The gain of the intensifier is adjustable through an analogical potentiometer. A support for the different filters is placed after the lens, to block the majority of surrounding light. Two optical filters are used to monitor chemiluminescence from OH radical with peak emission at 309 nm (Andover *310FS10-50*, $\tau_{max} = 17.40\%$, $\bar{\lambda} = 311.142$ nm) and CH radical with peak emission at 431 nm (Andover *430FS10-50*, $\tau_{max} = 50.76\%$, $\bar{\lambda} = 430.850$ nm). The chemically excited radicals are henceforth denoted OH* and CH*, respectively.

The focal distance was set to the minimal supported by the lens, in order to have the highest possible resolution of 56.51 pix/mm ($res = 17.70\,\mu$m/pix). The final captured area had an approximate size of 13×27mm. A $f/16$ aperture and an exposure time of 10 ms were used. Similarly to what was done in PIV, the acquisitions were conducted in a dark environment to reduce image noise and enhance contrast.

All the fuels mentioned in Table 2 were studied in this analysis. For each of them, two equivalence ratios and two Reynolds numbers were chosen: $\phi = \{0.7, 0.9\}$ and $Re = \{200, 300\}$. For BG100, the range of flame conditions was extended to include $\phi = \{0.8, 1.0\}$ for $Re = 200$.

Prior to all acquisitions, an image intensifier gain for each OH* and CH* was set. The gains defined were maintained across all tests, to permit the comparison between results. The gain was increased until pixels started to saturate for the flame condition with stronger chemiluminescence, to have the best image contrast possible for the weaker flames. When using the image intensifier, one should be careful not

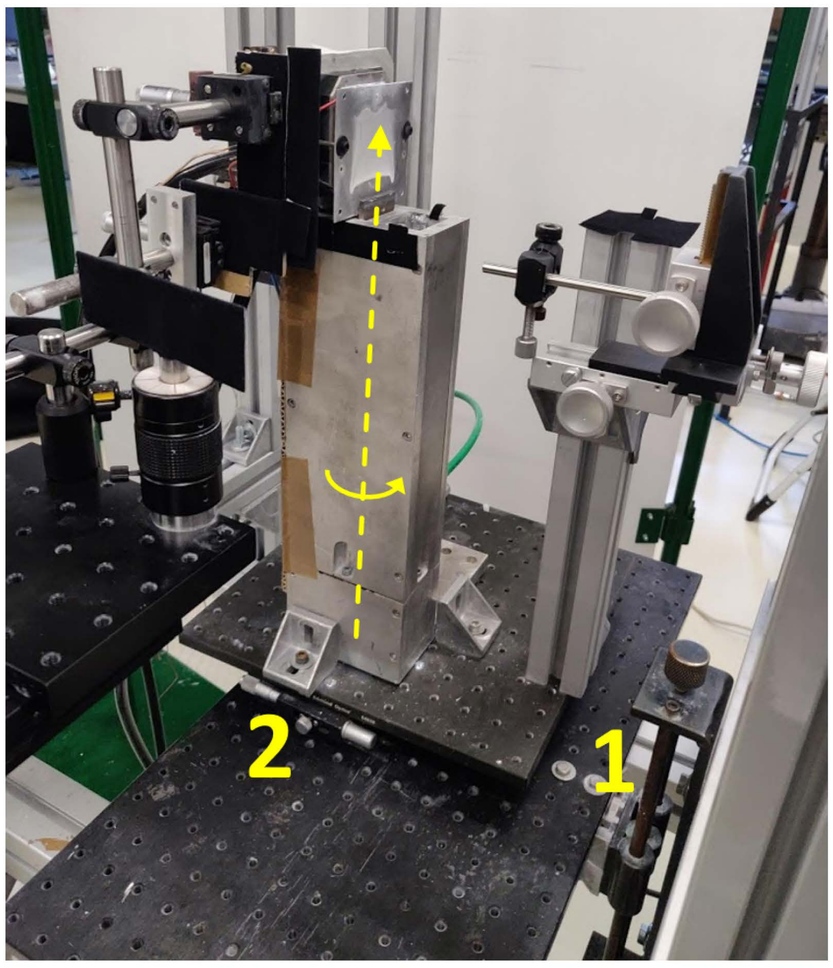

Figure 9: Equipment is fixed in platforms capable of y axis (1) translation and (2) precise rotation.

to operate it with small gains: that would imply to increase camera aperture and let more light to enter in the lens, which could burn the photocathode of the image intensifier. In order to have a more precise estimation of d_q, 30 images were captured at a rate of 5 Hz for each flame condition. A 5 min interval was kept between acquisitions for the system to reach steady state conditions.

The accurate measurement of quenching distance d_q relies on (i) correct calibration of setup (ii) information of wall position x_{wall}, and (iii) location of flame front boundary closest to the wall $x_{flm,0}$:

$$d_q\,[\mu\text{m}] = \left(x_{flm,0}\,[\text{pix}] - x_{wall}\,[\text{pix}]\right) \times res\,[\mu\text{m/pix}] \quad (12)$$

In the following sub-chapters, methods to accomplish these requirements are described.

5.1. Alignment and wall coordinate

Prior to image acquisitions, a series of steps were carried out to ensure that the wall and camera were aligned with a precision down to the tenth of degree. To determine quenching distance, this alignment process is crucial: a 1° angle misalignment can represent a deviation about 350 µm in the estimation of d_q. Therefore, the setup is mounted in a movable cart endowed of precise y translation and rotation movements, shown in Figure 9. At the end, this method permits (besides the alignment) the calculation of image resolution and exact determination of wall pixel location (x_{wall} coordinate).

The method was adapted from the one used by Häber and Suntz [9] and uses a small ball bearing sphere, with diameter $D_{sphere} = 10.3$ mm, that gently touches the wall (Figure 10) and is supported by small rod. Unlike a rectangular shape, the spherical shape can be identified even if partially hidden. This shape identification is done using the Hough

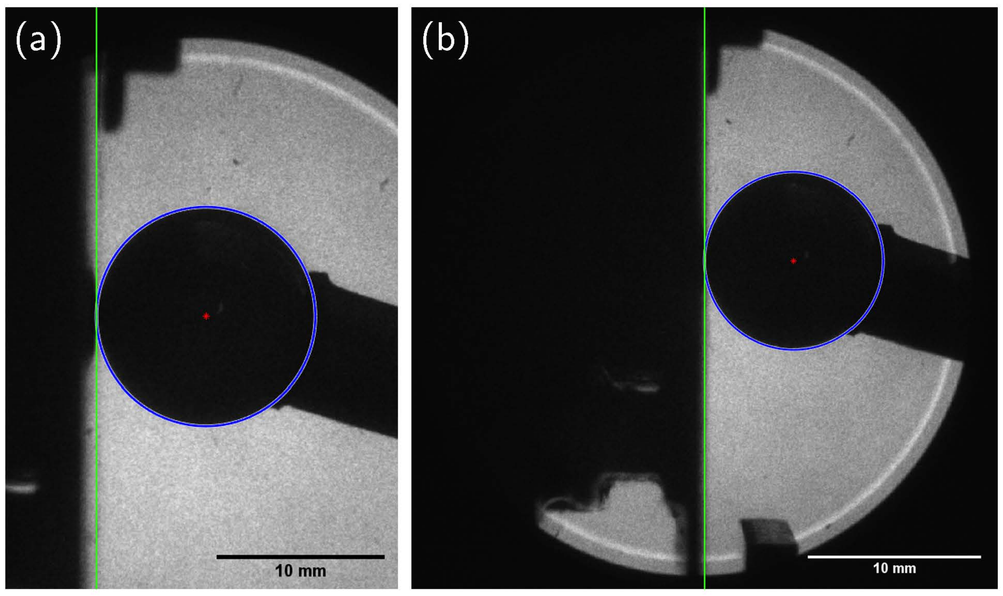

Figure 10: Cropped photos of sphere touching the wall at $z = 0$, for a (a) not yet aligned and (b) aligned setup; sphere edges and centers are identified and the vertical thin line represents the coordinate where the sphere touches the wall, *i.e.* x_{wall}.

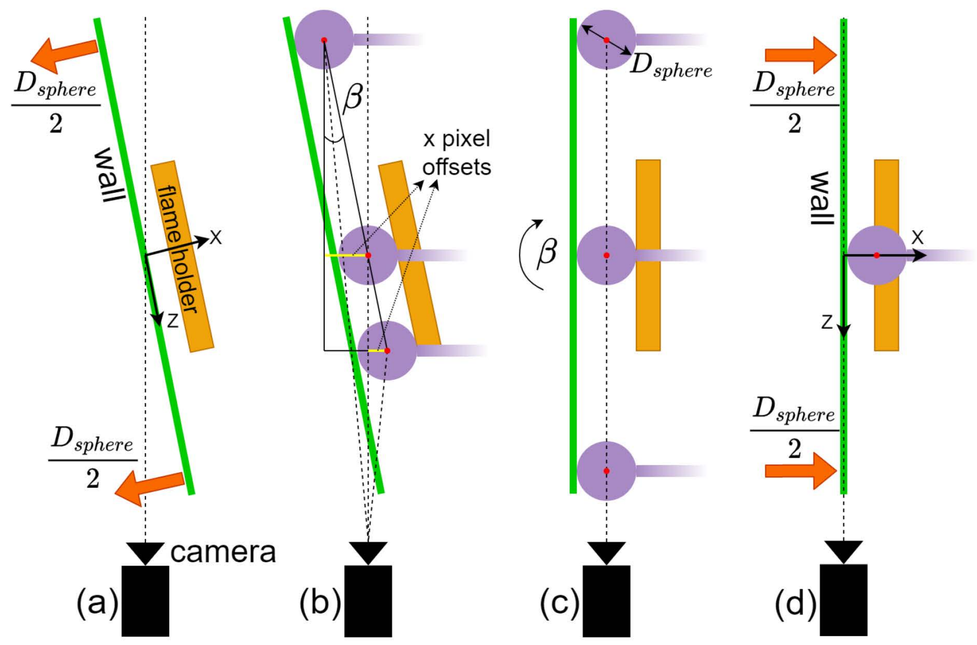

Figure 11: Camera and wall alignment involves different steps (a-d); the sphere of diameter D_{sphere} is used for perceiving the wall surface; at the end, the wall surface should be perpendicular to the lens (misalignment angle $\beta \approx 0$) and in the half-width of the image.

transform in MATLAB image analysis toolbox, which returns the sphere center and radius. For these images taken during alignment, the camera aperture was set to the smallest one ($f/32$), to obtain silhouette shapes with sharper edges and facilitate image processing.

Figure 11 contains, from left to right, a scheme with different steps followed during the alignment. The process can be divided in six main steps:

1 The wall was moved to the left a distance equal to the radius of the sphere ($\Delta x = -D_{sphere}/2$). Then, with the sphere touching the wall, its center was located at the coordinate where the wall surface once was (Figure 11a).
2 With the sphere touching the wall at $z = 0$, the setup must be moved until the center of the sphere was close to the half-width of the image captured. This made, at the end of the alignment, the wall surface to be centered in the camera images.
3 The sphere was moved along z coordinate (Figure 11b) and pictures were taken at each position; the z coordinate displacement should be maintained relatively

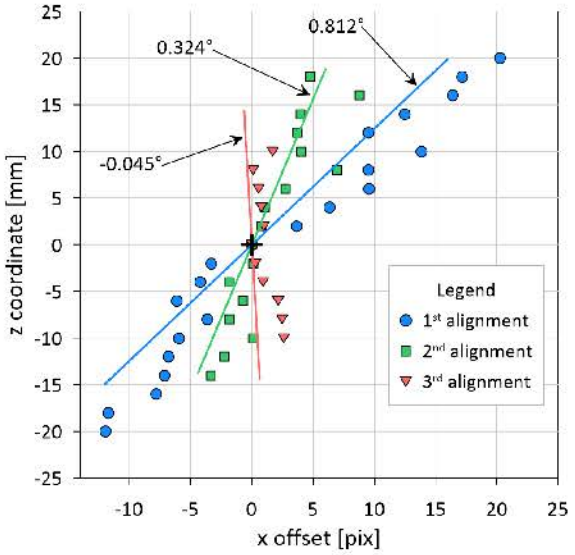

Figure 12: Sphere center offset for different z coordinates along the wall, in consecutive alignments. From the 1st alignment to the 3rd one, the misalignment angle β was reduced down to 0.045°.

small (in the present work it was no more than 20 mm), before optical aberrations preclude the assumed linear relation between pixel horizontal distances and z coordinate, along the wall planar surface.

4 The images obtained in the previous step were processed: contrast was maximized to facilitate the identification of spherical shape using Hough transform, and sphere center coordinates were determined for each image.

5 The misalignment angle β was estimated from pixel horizontal offsets, calculated at each z coordinate; if it was not small enough (the objective was set to 0.14° in the present work[1]), corrections were made using millimetric angle adjuster and we went back to step 3; otherwise, we proceeded to the next step. At this point, although the evaluated sphere radius varies with z coordinate, the sphere center remains at the same x pixel if $\beta \approx 0$ (Figure 11c). The image in Figure 10a was taken after this step.

6 Lastly, the wall was moved to its final position (moved $D_{sphere}/2$ to the right); the wall surface was then perpendicular to the camera lens and close to the half-width of image captured (Figures 10b and 11d).

The sphere z coordinates were varied every 2 mm. The angle of misalignment was estimated using linear fitting to the data points, shown in Figure 12. When aligned, x_{wall} pixel coordinate (identified with vertical lines in Figure 10) is obtained using the evaluated sphere center coordinate and radius. Image resolution is evaluated as well, from $res = D_{sphere}[\mu m]/D_{sphere}[pix]$.

[1] for estimated quenching distance errors associated below 50 µm

5.2. Chemiluminescence images processing

There are multiple methodologies for identifying flame front. Some authors use the HRR and its derivative ∇HRR [10]. Others, base themselves in temperature profiles and heat fluxes near the wall [11, 12]. The concentration and/or molar fraction of species (CO_2, CH, CH_4) [13, 14] or even radicals fluorescence (OH usually) [11, 10] can also be employed to anchor the flame front position. In the present work, another common methodology already employed in similar studies [9], was chosen.

The flame front was traced using the points where the concentration of OH* and CH* reached 50% of their maximum value. It was shown that there is a proportional relation between radicals concentration and their chemiluminescence intensity [15]. The use of the 50% intensity presents a robust technique, since this region of the flame has a better signal-to-noise ratio and is less sensitive to small perturbations in the flame, that could increase the uncertainty of the measurement.

Independently of the method chosen, its applicability and validity for all the conditions tested should be a major concern. Numerical simulations of a one-dimensional, adiabatic flame confirmed that OH* and CH* peak concentrations are consistent with maximum HRR location for BG and BG + H_2 flames, endorsing the method chosen to identify the flame front. These simulations are based on GRI-Mech 3.0 database, which is supplemented with chemiluminescent species kinetics [15], to simulate the concentrations of excited radicals. Flame was simulated with initial conditions $T_u = 298.15\,K$, $p = 1atm$.

The outcome of image processing techniques applied to an OH* chemiluminescence photo can be seen in Figure 13. The process involves image magnification by a factor of five (linear interpolation), to increase its resolution, trace the flame front with sub-pixel precision, and thus enable a better statistical description of d_q (since its value will not be locked in multiples of pixel resolution). The pixels whose value is greater than $I_{max}/2$ define the region of the flame front. d_q can now be computed from the most left pixel and the well determined wall position coordinates (Equation 12).

Concentration of OH* was known to be a good indicator of the location and intensity of the HRR and that the relation between radical concentration and HRR was approximately linear [16]. This was of major importance to give a physical interpretation of the pixel intensity from OH* chemiluminescence (I_{OH}), and hence extend the meaning of our results. Since the flame surface is projected on z axis, I_{OH} can be translated into the total volumetric heat generated $\dot{q}'''$ along the flame length (in z direction):

$$I_{OH} \propto \int_{-l/2}^{l/2} \dot{q}'''\, dz \qquad (13)$$

where l is the burner length (approximately equal to the flame length). If dimensions are to be attributed to I_{OH}, it represents a power per surface area *i.e.* $[W/m^2]$.

For the results analysis, two useful variables related to the heat release were defined: heat release thickness $\delta_{q,OH}$

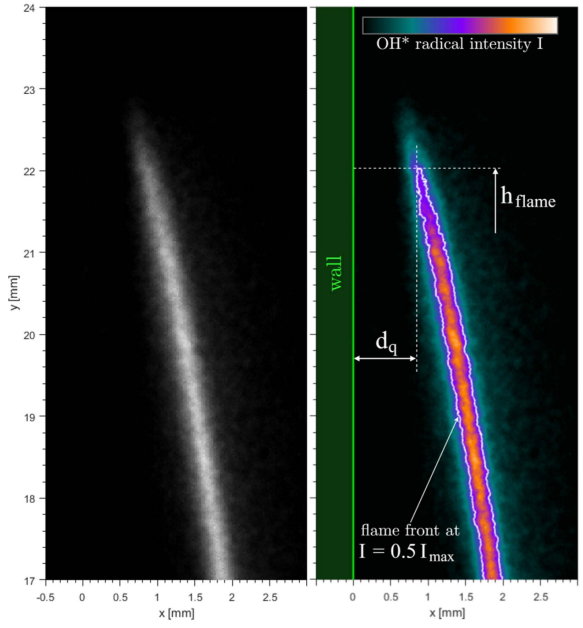

Figure 13: Photo of a BG60 20%H_2 flame ($\phi = 0.9, Re = 300$) using OH* radical (left) and the correspoding processed image (right), with the flame front position outlined in white; it corresponds to the pixels where the radical intensity reach 50% of the maximum; the quenching distance is determined knowing the wall pixels location (x_{wall}) *a priori*.

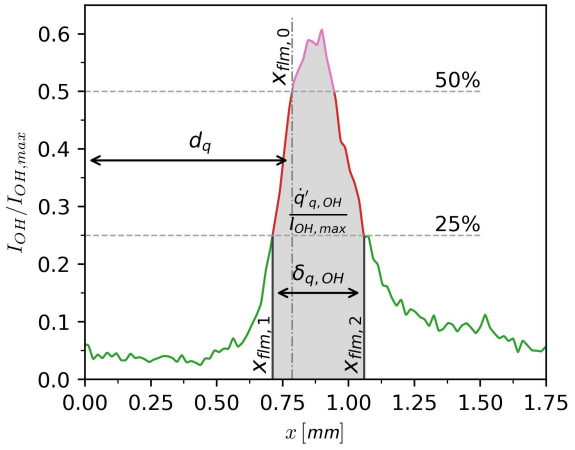

Figure 14: Calculation of relevant variables (d_q, heat release thickness $\delta_{q,\mathrm{OH}}$, and heat release in quenching $\dot{q}'_{q,\mathrm{OH}}$) from OH* chemiluminescence from profile of normalized pixel intensity in the x direction and at the height of the pixel defining quenching point.

and heat release in quenching $\dot{q}'_{q,\mathrm{OH}}$. Figure 14 shows how those can be computed numerically from the profile of I_{OH} at the y coordinate of quenching point.

The heat release thickness is defined as the distance between the points where normalized pixel intensity rise above ($x_{flm,1}$) and drops below ($x_{flm,2}$) 25%:

$$\delta_{q,\mathrm{OH}} = x_{flm,2} - x_{flm,1} \tag{14}$$

where, given the assumptions and the close relation with HRR, most of the combustion heat is produced. Those points are at the same height as of the pixel that defines quenching distance.

As for the heat release in quenching, it is determined from the integral of pixel intensity, in the same interval that defines $\delta_{q,\mathrm{OH}}$:

$$\dot{q}'_{q,\mathrm{OH}} = \int_{x_{flm,1}}^{x_{flm,2}} I_{\mathrm{OH}}\, dx \tag{15}$$

and thus is an indicative figure of the amount of energy released in that area, per unit length in y direction $\left[\mathrm{W/m}\right]$.

6. Uncertainties

In this section, uncertainty of any result or measurement with expected value a presented as $a \pm u_{95\%}$, correspond to the upper and lower bounds of the 95% confidence interval of possible values. If the uncertainty is presented as a percentage $a \pm u_r\%$, it refers to the relative uncertainty, calculated from:

$$u_r = \frac{u_{95\%}}{a} \times 100 \tag{16}$$

Guidelines advised from Abernethy et al. [17] about quantifying uncertainties were followed. Populations of measurements were assumed normal distributed (except for PIV results). Student's t-distribution was used for populations smaller than 30, with an adequate degree of freedom. Table 3 contains the absolute and relative uncertainties of different measured/estimated quantities and dependent results. Whenever possible, average and maximum uncertainties are presented. Sources of systematic errors have a single value presented in the table, corresponding to the respective bias. All the other variables with multiple columns correspond to statistical sources of error.

The flowmeters uncertainty presented in datasheet depend on the flowmeter capacity and on the value of setpoint. This uncertainty has a direct impact in Re, ϕ and P_{flm}. In general, as the setpoint diminishes, the final relative uncertainty of the result increases.

For TEG power yielded P_{TEG}, the sources of error result from the systematic and statistical errors associated with acquisition board reading, from the statistical uncertainty when determining $R_{e,load}$, and from the relation between U_{cc} and U_m.

To evaluate cross correlation uncertainty in PIV analysis, a radial velocity error is deduced using a DynamicStudio's tool based on the quantification of signal-to-noise ratio [18]. Histograms with the uncertainties of all image interrogation areas were then analyzed to compute the most expected and 95% confidence values, which are presented in Table 4. An expected value E is used to characterize, instead of the typical average value, the non-normal probability distribution.

The pixel resolution does not have a significant impact in the PIV uncertainty. The diameter of the Airy disk, D_{Airy}, produced from small particles Mie scattering, can be calculated from the magnification factor M, camera f number

Table 3
Uncertainties from sources of error and their impact in important results; entries with unique value correspond to systematic errors; entries without a value for u_r do not have a reference value

			$u_{95\%}$	u_r	
			max	avg	max
Flame Condition and Water Flow Rate	$\dot{V}_{CH_4}$	[SLPM]	9.3e-3	0.45%	0.83%
	$\dot{V}_{CO_2}$	[SLPM]	5.3e-3	0.84%	3.09%
	$\dot{V}_{H_2}$	[SLPM]	3.2e-3	0.26%	1.07%
	$\dot{V}_{air}$	[SLPM]	0.188	1.11%	1.70%
	Re		5.395	1.97%	2.93%
	ϕ		0.021	1.21%	2.12%
	P_{flm}	[W]	5.547	0.43%	0.75%
	$\dot{V}_{H_2O}$	[SLPM]	0.046	3.70%	3.70%
Power and Temperature	$R_{e,load}$	[Ω]	9.4e-4	0.34%	0.34%
	U_{cc}	[V]	4.9e-2	1.51%	4.89%
	P_{TEG}	[W]	0.352	3.10%	9.81%
	Temperature	[°C]	0.18	-	0.95%
PIV	pixel resolution			≈ 0	
	correlation radial error	[mm/s]	257	5.40%	5.49%
Quenching Distances	pixel resolution	[µm]		8.85	
	optical aberrations	[µm]		≈ 0	
	x_{wall}	[µm]	21.1	-	-
	flame front position	[µm]	138.8	5.63%	10.11%
	quenching distance d_q	[µm]	139.0	5.71%	10.13%

Table 4
PIV correlation radial uncertainty for four representative flame conditions of BG100; the statistics presented take into account the uncertainty associated with each interrogation area in the image; the expected value (letter E) was used to describe the probability distribution of values

		V [m/s]	absolute error [mm/s]		relative error	
Re	ϕ	E	E	$u_{95\%}$	E	u_r
200	0.7	2.16	14	34	2.24%	5.49%
200	0.8	2.18	70	172	2.16%	5.29%
300	0.7	3.03	103	252	2.18%	5.34%
300	0.9	3.13	105	257	2.23%	5.46%

($f\#$) and the laser light wavelength λ [7]:

$$D_{Airy} = 2.44 f\# \cdot (M+1) \cdot \lambda \quad (17)$$

The Al_2O_3 particles produce an Airy disk with a diameter of 191 µm, which is about 6.35 times the pixel resolution, making the used resolution small enough for the software to compute the intensity peak with subpixel precision and proving that the contribution of this source of error to the global uncertainty is negligible.

Finally, the precision of measurement of quenching distances has systematic and statistical errors associated. The systematic errors arise mainly from the pixel resolution and the lens optical aberrations. Optical aberrations can be neglected since the quenching region is located at half-width of the image and hence d_q does not suffer significant distortions. The statistical errors arise from the uncertainty associated with the determination of x_{wall} (20 values measured at the same z coordinate) and flame tip positions (evaluated from the 30 flame images).

7. Conclusions

In this paper important experimental methodologies to study the flame-wall interaction of premixed biogas+H_2 flames were presented. FWI is important for flame stabilization in small scale combustion chambers and for heat transfer from flame to TEG, to improve power yielded. Using PIV and chemiluminescence of CH* and OH* radicals, information about flow field, quenching distances and heat release rate can be obtained.

The main findings related with the analysis of obtained results are:

1. TEG power increases largely with ϕ and slightly with Re. In opposition to TEG efficiency, heat transfer efficiency varied significantly (more than 3 times with different flame conditions tested) and influenced system efficiency the most.
2. For a flame in SWQ, the decrease in gases density in the flame front induces the deviation of streamlines farther away from the wall, right after the quenching region. That reduces velocity (and temperature) gradients in the vicinity of the wall, inhibiting the heat transfer and causing most of the heat to be lost to the atmosphere.
3. Adding H_2 to BG is very effective to increase power harvested in the TEG module and to decrease flame quenching distances, essential for better flame stabilization and heat transfer in downsized combustion chambers. The lower the grade of BG fuel blend, the higher the impact of H_2: with 20% addition to BG60, P_{TEG} improved by 10% on average, and quenching distances were reduced by 18%.
4. For the close relation with HRR, chemiluminescence intensity from OH* can be used to diagnose d_q. It was found (i) the intensity of chemiluminescence to be proportional to $d_q^{-0.45}$ for lean mixtures of any BG+H_2 fuel blends tested and (ii) convection not to be negligible for heat transfer, in the quenching region.

Nomenclature

Greek symbols

β	Camera - Al plate misalignment angle
Δt	PIV time between pulses
κ	Thermal conductivity
λ	Wavelength of electromagnetic wave
ν	Kinematic viscosity
ρ	Density
ϕ	Air-fuel mixture equivalence ratio
χ	Molar fraction

Roman symbols

D	Diameter
d_q	Quenching distance
I	Intensity of image pixel
I_e	Electric current
$\mathrm{IA}_{x,y}$	PIV interrogation area width, height
l	Burner slit length
m	Mass
o_{IA}	PIV interrogation area overlap
P_{flm}	Flame power
P_{TEG}	Power yielded by TEG
q	Heat exchange rate
$\dot{q}$	Heat generation
$R_{e,load}$	Electrical circuit load resistance
$R_{e,TEG}$	TEG internal electrical resistance
Re	Reynolds number
res	Pixel resolution
T	Temperature
$u_{95\%}$	Uncertainty with 95% confidence level
u_r	Relative uncertainty
U_m	Voltage measured in acquisition board
U_{oc}	Open circuit voltage
U_{cc}	Closed circuit voltage
V	Velocity
$\dot{V}$	Volumetric flow rate
x, y, z	Cartesian coordinates
w	Burner slit width
Y_F	Fuel mass fraction

Subscripts

i	initial conditions
f	final conditions
ad	adiabatic conditions
flm	with respect to flame
b	referring to burnt gases
u	referring to unburnt gases
$wall$	referring to Al plate surface
q	relative to quenching
C	TEG cold side
H	TEG hot side
max	maximum
min	minimum
mix	referring to air-fuel mixture

References

[1] IEA, World energy outlook, 2020. URL: https://www.iea.org/sankey/.

[2] M. Tabatabaei, H. Ghavinati, Biogas: Fundamentals, Process, and Operation., Springer, Cham, Switzerland, 2018. doi:10.1007/978-3-319-77335-3.

[3] D. Champier, Thermoelectric generators: A review of applications, Energy Conversion and Management 140 (2017) 167–181. doi:10.1016/j.enconman.2017.02.070.

[4] D. G. Goodwin, H. K. Moffat, R. L. Speth, Cantera: An object- oriented software toolkit for chemical kinetics, thermodynamics, and transport processes, 2017. URL: https://cantera.org.

[5] G. Smith, D. Golden, M. Frenklach, N. Moriarty, B. Eiteneer, M. Goldenberg, C. Bowman, R. Hanson, S. Song, W. Gardiner, Gri-mech 3.0, chemical kinetic mechanism, 1999. URL: http://combustion.berkeley.edu/gri-mech/.

[6] F. Cheng, Calculation Methods for Thermoelectric Generator Performance, in: M. Nikitin, S. Skipidarov (Eds.), Thermoelectrics for Power Generation - A Look at Trends in the Technology, 2016. doi:10.5772/65596.

[7] M. Raffael, C. Willert, S. T. Wereley, J. Kompenhans, Particle Image Velocimetry - A Practical Guide, 3 ed., Springer, 2007. doi:10.1007/978-3-319-68852-7.

[8] Dantec Dynamics, DynamicStudio User's Guide, Skovlunde, Denmark, 2016.

[9] T. Häber, R. Suntz, Effect of different wall materials and thermal-barrier coatings on the flame-wall interaction of laminar premixed methane and propane flames, International Journal of Heat and Fluid Flow 69 (2018) 95–105. doi:10.1016/j.ijheatfluidflow.2017.12.004.

[10] H. Kosaka, F. Zentgraf, A. Scholtissek, C. Hasse, A. Dreizler, Effect of Flame-Wall Interaction on Local Heat Release of Methane and DME Combustion in a Side-Wall Quenching Geometry, Flow, Turbulence and Combustion 103 (2019) 181–192. doi:10.1007/s10494-019-00090-4.

[11] C. Jainski, M. Rißmann, B. Böhm, J. Janicka, A. Dreizler, Sidewall quenching of atmospheric laminar premixed flames studied by laser-based diagnostics, Combustion and Flame 183 (2017) 271–282. doi:10.1016/j.combustflame.2017.05.020.

[12] A. Gruber, R. Sankaran, E. R. Hawkes, J. H. Chen, Turbulent flame-wall interaction: A direct numerical simulation study, Journal of Fluid Mechanics 658 (2010) 5–32. doi:10.1017/S0022112010001278.

[13] S. Ganter, A. Heinrich, T. Meier, G. Kuenne, C. Jainski, M. C. Rißmann, A. Dreizler, J. Janicka, Numerical analysis of laminar methane–air side-wall-quenching, Combustion and Flame 186 (2017) 299–310. doi:10.1016/j.combustflame.2017.08.017.

[14] A. Heinrich, F. Ries, G. Kuenne, S. Ganter, C. Hasse, A. Sadiki, J. Janicka, Large Eddy Simulation with tabulated chemistry of an experimental sidewall quenching burner, International Journal of Heat and Fluid Flow 71 (2018) 95–110. doi:10.1016/j.ijheatfluidflow.2018.03.011.

[15] F. M. Quintino, T. P. Trindade, E. C. Fernandes, Biogas combustion: Chemiluminescence fingerprint, Fuel 231 (2018) 328–340. doi:10.1016/j.fuel.2018.05.086.

[16] C. S. Panoutsos, Y. Hardalupas, A. M. Taylor, Numerical evaluation of equivalence ratio measurement using OH* and CH* chemiluminescence in premixed and non-premixed methane-air flames, Combustion and Flame 156 (2009) 273–291. doi:10.1016/j.combustflame.2008.11.008.

[17] R. B. Abernethy, R. P. Benedict, R. B. Dowdell, Asme Measurement Uncertainty, Journal of Fluids Engineering 107 (1985) 161–164. doi:10.1115/1.3242450.

[18] J. J. Charonko, P. P. Vlachos, Estimation of uncertainty bounds for individual particle image velocimetry measurements from cross-correlation peak ratio, Measurement Science and Technology 24 (2013) 065301. doi:10.1088/0957-0233/24/6/065301.